Regional Guidance-Based Multiscale Joint Filtering Model for SAR Images

Chuang Sun[®], Fengcheng Guo[®], Zhaoling Hu, Lianpeng Zhang[®], Wensong Liu[®], and Tingting Huang

Abstract—Synthetic aperture radar (SAR) imaging systems are characterized by their all-weather and day-and-night capabilities, enabling the acquisition of high-resolution ground imagery. However, the presence of speckle significantly hinders the effective utilization of SAR images. In this article, a novel coherent speckle suppression method was proposed, leveraging the statistical characteristics and texture information inherent in SAR data. To account for the texture features of SAR images, a new guide map termed regional guided images-was developed and integrated into the nonlocal means framework to implement a region-based speckle reduction approach. Double hesitant neutrosophic set functions were constructed by incorporating both the statistical distribution and multiscale features of SAR images. In addition, surface variation was introduced to model the nonlocal self-similarity properties of SAR data. By embedding this framework into nonlocal filtering models, the proposed method effectively achieved coherent speckle suppression while preserving structural details. Comparative experiments on real SAR images demonstrate that the proposed method outperforms several state-of-the-art techniques. It achieved a favorable balance between speckle reduction and edge preservation, as evidenced by both visual assessments and quantitative evaluations. These results verify the effectiveness and advancement of the method in SAR image speckle suppression.

Index Terms—Hesitant neutrosophic set (HNS), multiscale filtering, regional guided images (RGIs), speckle reduction, synthetic aperture radar (SAR).

I. INTRODUCTION

YNTHETIC aperture radar (SAR), a prominent form of active remote sensing, has been widely employed in military applications, surveying and mapping, and disaster monitoring due to its unique capability for all-weather, day-and-night observation [1], [2], [3], [4]. However, the inherent fidelity of SAR imagery is unavoidably degraded by speckle, which arises from the coherent superposition of backscattered radar signals and

Received 29 May 2025; revised 21 August 2025; accepted 2 October 2025. Date of publication 6 October 2025; date of current version 17 October 2025. This work was supported in part by the National Natural Science Foundation of China under Grant 62101219 and 62201232, in part by the Jiangsu Provincial Natural Science Foundation of China under Grant BK20210921 and Grant BK20201026, in part by the "343" Industrial Development Project for University in Xuzhou under Grant gx2023010, and in part by the Social Welfare Project in Xuzhou City under Grant KC23304. (Corresponding author: Fengcheng Guo.)

Chuang Sun, Fengcheng Guo, Zhaoling Hu, Lianpeng Zhang, and Wensong Liu are with the School of Geography, Geomatic and Planning, Jiangsu Normal University, Xuzhou 221116, China (e-mail: 2020231583@jsnu.edu.cn; fchguo@jsnu.edu.cn; huzhaoling@jsnu.edu.cn; zhanglp2000@126.com; liuwensongupc@163.com).

Tingting Huang is with the School of Institute of Surveying, Mapping and Geoinformation, Guilin University of Technology, Guilin 541004, China (e-mail: 1020232083@glut.edu.cn).

Digital Object Identifier 10.1109/JSTARS.2025.3617942

significantly impairs subsequent interpretation tasks [5], [6], [7], [8]. Consequently, the development of reliable speckle suppression algorithms for SAR images remains critically important.

Suppressing speckle while preserving the intrinsic information of SAR images has remained a central challenge in SAR image processing. In recent years, researchers worldwide have dedicated considerable effort to this issue, leading to the development of numerous innovative methods and algorithms. Early speckle reduction techniques primarily relied on multilook processing, which, although effective at reducing coherent speckle, often resulted in diminished spatial resolution. However, with the expansion of SAR applications and the growing demand for high-resolution imagery, spatial domain filtering has gradually supplanted traditional multilook approaches as the preferred method [9]. Spatial domain filtering utilizes sliding windows to compute local statistical measures and suppress speckle by exploiting pixel-level correlations. While effective in homogeneous regions, this approach frequently blurs edges and degrades texture details. Notable algorithms in this category include Lee filtering [10], extended Lee filtering [11], Kuan filtering [12], Frost filtering [13], and Gamma-MAP filtering [14]. To address the limitations of spatial domain methods, various transform domain filtering techniques have been introduced, such as wavelet transform [15], ridgelet transform [16], curvelet transform [17], contourlet transform [18], and shearlet transform [19]. These methods operate by filtering the image in the transform domain, allowing for more effective representation and suppression of speckle while preserving structural details. However, this process often required complex shearlet transformations, which could result in smooth transitions, blurred edges, and the emergence of pseudo-Gibbs artifacts. To improve filtering performance, anisotropic diffusion (AD) techniques were introduced into SAR image de-speckling. AD filters suppressed speckle primarily by computing pixel-wise diffusion coefficients and applying partial differential equations to filter images across multiple scales. Representative algorithms in this category included speckle reducing anisotropic diffusion filtering (SRAD) [20], detail preserving anisotropic diffusion filtering [21], and pixel difference function-local entropy-speckle reducing anisotropic diffusion filtering [22]. Although AD filters achieved effective speckle suppression, they often caused more pronounced edge blurring and introduced artifacts. Moreover, their performance was highly sensitive to parameter selection such as the diffusion coefficient and the number of iterations which varied considerably depending on the characteristics of the input image.

In recent years, deep learning methods have attracted significant attention in the field of SAR image denoising. Representative algorithms included SAR-convolutional neural network [23], SAR-dilated residual network [24], multiobjective network (Monet) [25], G-Monet [26], multiscale feature adaptive enhancement network [27], and adaptive noise estimation and despeckling network [28]. These approaches leveraged the powerful feature extraction capabilities of neural networks to effectively suppress speckle in SAR images. However, most supervised deep learning algorithms were designed to handle specific speckle levels, and their generalization performance was highly dependent on the availability of large-scale training datasets. Moreover, real SAR images often differed substantially from synthetic training data in terms of speckle characteristics and scene complexity. This domain gap limited the performance of deep learning-based filters in complex, real-world scenarios, often resulting in suboptimal despeckling outcomes.

In 2005, Buades et al. [29] introduced the nonlocal means (NLMs) filtering algorithm for denoising additive speckle images, providing a novel framework for speckle suppression in SAR imagery. The NLM algorithm exploited nonlocal similarity by identifying pixel patches similar to a target patch and computing their weighted similarity for effective despeckling. However, the traditional similarity measurement in NLM was relatively limited and often failed to achieve satisfactory performance in complex terrain scenarios. To overcome these limitations, extensive research was conducted both domestically and internationally. Feng et al. [30] proposed a method that utilized the probability density function (pdf) of the intensity ratio between patches to assess similarity. While this technique effectively suppressed coherent speckle in homogeneous regions, it showed limited capability in preserving edge features and retaining point scatterers. Deledalle et al. [31] introduced a probabilistic patch-based (PPB) despeckling algorithm for SAR images, which measured similarity based on the probabilistic correspondence between image patches, deviating from the conventional Euclidean distance metric. This approach assumed that coherent speckle in SAR multilook images followed a generalized Gamma distribution. Although the algorithm demonstrated strong performance in speckle smoothing and edge preservation, it also tended to produce noticeable pseudo-texture artifacts. Zhong et al. [32] later proposed a SAR de-speckling method based on Bayesian NLMs, introducing a statistical distance metric to evaluate similarity between image blocks. This approach demonstrated excellent speckle suppression capabilities. Parrilli et al. [33] developed a method to determine the optimal local linear minimum mean square error in the wavelet domain and successfully applied block-matching 3-D to SAR despeckling (SAR-BM3D). Cozzolino et al. [34] further advanced this work by introducing the fast adaptive nonlocal SAR denoising algorithm (FANS), which offered higher speckle suppression efficiency but was susceptible to over-smoothing. Ferraioli et al. [35] introduced the concept of ratio blocks, achieving speckle suppression based on statistical similarity between blocks. By incorporating AD techniques, they improved edge and texture preservation. Vitale et al. [36] proposed a technique utilizing guided images to perform SAR image de-speckling by

integrating SAR and registered optical images. Although this method achieved superior speckle reduction, it presented challenges in data acquisition. Ni and Gao [6] developed the Bayesian NLM generalized guided filter, which enhanced SAR despeckling by combining Bayesian inference with NLMs and guided filtering.

Inspired by the strengths and insights of the previously discussed joint methods, this study conducted a comprehensive investigation into the multiscale characteristics of SAR images. We introduced the concept of a regional guidance image and implemented multiscale filtering strategies, which led to the development of an innovative speckle suppression algorithm for SAR imagery. The primary contributions and novelties of this research are summarized as follows.

- A novel regional guidance multiscale joint filtering method (RG-MSJF) was proposed. In the initial phase of constructing regional guided images (RGIs), advanced edge detection operators were incorporated. These operators effectively captured and highlighted the edge features of the image, thereby establishing a strong foundation for the subsequent filtering processes applied to regional images.
- 2) The similarity metric of the NLMs algorithm was redesigned by integrating three distinct modules. The first module calculated the correlation coefficients between the target patch and similar patches, emphasizing the importance of global information in the filtering process. In the second and third modules, we designed surface variational and double hesitant neutrosophic sets (HNSs), respectively, to enhance the preservation of local edge information throughout the filtering process.
- 3) The statistical characteristics of SAR images were thoroughly investigated, and a novel edge detection model based on the theory of double HNSs was proposed. This model was designed to overcome the limitations of the traditional NLM algorithm, particularly its reliance on a single similarity measurement index and its tendency to cause significant edge information loss. By introducing this innovative approach, the model achieved improved despeckling performance while preserving critical edge details.

The rest of this article is organized as follows. Section II introduces the speckle model for SAR images and presents the complete RG-MSJF algorithm. Section III describes the quantitative and visual experiments conducted to evaluate the algorithm and discusses the influence of several key parameters on the filtering results. Section IV conducts validation experiments on the proposed algorithm, selecting representative land features on SAR images. Finally, Section V summarizes the contributions and findings of this study.

II. RELATED WORKS

A. SAR Statistical Model

Let Y represent the SAR images with speckle, and X denote the corresponding speckle-free amplitude images; the speckle n

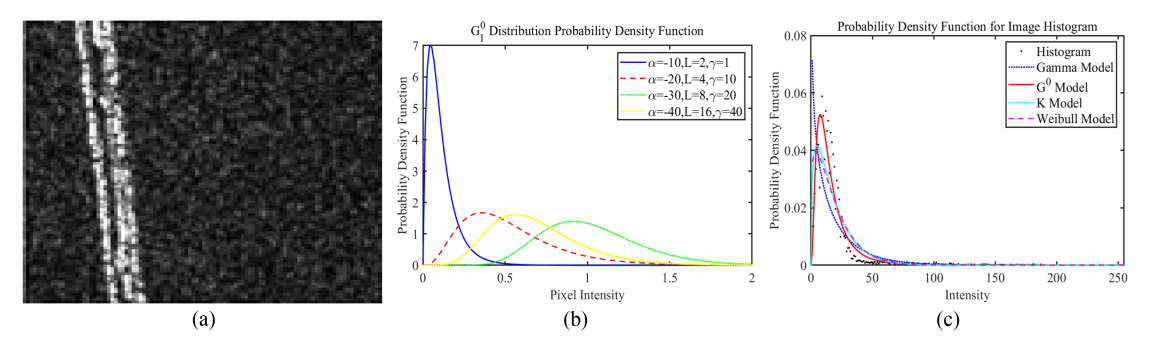


Fig. 1. Fitting SAR images with different statistical models. (a) Real SAR image. (b) Effect of parameters on the G_I^0 distribution. (c) Histogram and fitted pdfs.

introduced by the coherent imaging process, is spatially correlated with each other according to the following equation:

$$Y(r,c) = X(r,c) \cdot n(r,c) \tag{1}$$

where r and c, respectively, represent the coordinates of pixels within the image domain $\Omega \subseteq \Re^2$. Under the hypothesis of fully developed speckle, the speckle in SAR images is commonly modeled as a Gamma distribution with a unit mean and a variance of 1/L, and L represents the number of looks. The pdf is modeled as follows:

$$P(N) = \frac{1}{\Gamma(L)} \cdot L^{L} N^{L-1} e^{-L \cdot N}, N > 0, L \ge 1$$
 (2)

where $\Gamma(\cdot)$ denotes the Gamma function. To characterize the statistical properties of SAR images, Frery et al. introduced the G^0 model [37]. This model assumes that the speckle component follows a Gamma distribution, while the terrain backscattering is modeled by an inverse Gamma distribution. These assumptions enable effective representation of both homogeneous and heterogeneous regions within SAR images. The pdfs of the G^0 distribution for amplitude and intensity SAR images are given as follows:

$$P_{A}^{G^{0}}\left(A;\alpha;\gamma;L\right) = \frac{2L^{L}\Gamma\left(L-\alpha\right)\gamma^{-\alpha}A^{2L-1}}{\Gamma\left(L\right)\Gamma\left(-\alpha\right)\left(\gamma+LA^{2}\right)^{L-\alpha}}$$
$$-\alpha,\gamma,L \geq 1, A > 0$$
$$P_{I}^{G^{0}}\left(I;\alpha;\gamma;L\right) = \frac{L^{L}\Gamma\left(L-\alpha\right)\gamma^{-\alpha}I^{L-1}}{\Gamma\left(L\right)\Gamma\left(-\alpha\right)\left(\gamma+LI\right)^{L-\alpha}}$$
$$-\alpha,\gamma,L \geq 1, A > 0. \tag{3}$$

Among these, A and I respectively represent amplitude and intensity SAR images; γ denotes the scale parameter; and α characterizes the roughness of the observed region. A smaller value of $-\alpha$ indicates higher homogeneity, whereas a larger value corresponds to greater heterogeneity. Fig. 1(b) illustrates the probability density function of the fitted G_I^0 distribution under various parameter settings. It is evident that as the parameter $\alpha \to \infty$, the G^0 distribution converges toward the Gamma distribution. Fig. 1(c) presents the results of fitting histograms derived from real high-resolution SAR images using several statistical models. Specifically, the G^0 distribution [38], Gamma

distribution [39], [40], K distribution [41], and Weibull distribution [42] are employed to approximate the pdf. To evaluate the effectiveness of these models, the Jensen-Shannon divergence (JSD) [43] is computed between the histograms of the fitted pdfs and the empirical SAR data. This metric provides a quantitative measure of similarity, with lower JSD values indicating a better fit. This can be modeled as follows:

$$\begin{split} \operatorname{JSD}\left(F|G\right) &= \frac{1}{2} \operatorname{KL}\left(F_{\mu}|\frac{F_{\mu} + G_{\mu}}{2}\right) + \frac{1}{2} \operatorname{KL}\left(G_{\mu}|\frac{F_{\mu} + G_{\mu}}{2}\right) \\ &= \frac{1}{2} \int \left(F_{\mu} \log \frac{2F_{\mu}}{F_{\mu} + G_{\mu}} + G_{\mu} \log \frac{2G_{\mu}}{F_{\mu} + G_{\mu}}\right) \! d\mu. \end{split} \tag{4}$$

Here, F and G denoted two distinct probability distributions. μ represents a random variable. KL represents the asymmetric distance between two probability distributions. The computed JSD values for each model are as follows: 0.0406 for the Gamma distribution, 0.0494 for the K distribution, 0.0695 for the Weibull distribution, and 0.0245 for the G^0 distribution. These results demonstrate that the G^0 model provides a significantly better fit to real SAR images compared to the other models. This conclusion is further supported by the visual evidence presented in Fig. 1(c). To validate the above findings with greater robustness, experiments were conducted using a selection of 50 representative real SAR images, including different land features such as mountains, rivers, cities, farmland, and roads. The outcomes revealed that the JSD value for the G^0 model was 1.7311, which is substantially lower than the values observed for the Gamma model, K model, and Weibull models—2.8585, 5.6079, and 3.6797, respectively. These results suggest that the G^0 model is particularly well suited for characterizing the statistical properties of SAR images, outperforming the other evaluated models in both visual and quantitative assessments.

B. Nonlocal Means Filter

Let $\Omega\subseteq\Re^2$ denote the domain of definition for the intensity SAR image $Y\colon\Omega\subseteq\mathbb{R}^2$. Let the speckled image be denoted as Y, the target patch for filtering as Q_ι , and the neighboring patches as P_κ , where ι,κ represent the central pixel positions of these patches, respectively. The term $w(P_\iota,Q_\kappa)$ denotes the similarity weight, which quantifies the degree of resemblance between

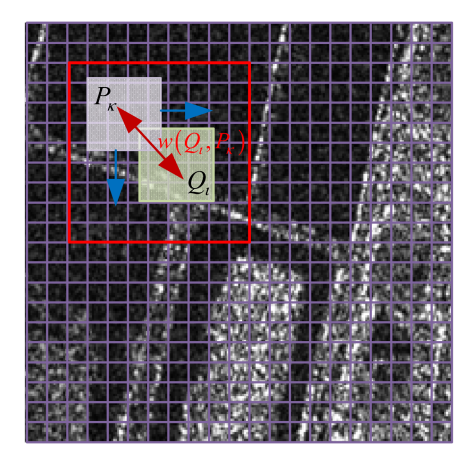


Fig. 2. Main concept of the NLM algorithm.

patches. The specific concept of NLM is shown in Fig. 2. Let Y(r,c) and $\operatorname{NL}(r,c)$ denote the pixel values at location (r,c) in the original and restored images, respectively. $\Omega_{r,c}$ represents the set of neighboring pixels of coordinate point (r,c). The NLM algorithm estimates $\operatorname{NL}(r,c)$ by computing a weighted average of pixel values across all patches within the search window in (r,c). The model is expressed as follows:

$$NL(r,c) = \frac{\sum_{\Omega_{r,c}} w(P_{\kappa}, Q_{\iota}) Y(r,c)}{\sum_{\Omega_{r,c}} w(P_{\kappa}, Q_{\iota})}$$
(5)

where

$$w(P_{\kappa}, Q_{\iota}) = \exp\left(-\frac{\|Y(Q_{\iota}) - Y(P_{\kappa})\|_{2,a}^{2}}{h^{2}}\right).$$
 (6)

The algorithm employed the Euclidean distance to quantify the similarity between two neighboring patches. Here, a>0 denoted the standard deviation of the Gaussian kernel. $\|\cdot\|$ represents absolute value operation. The parameter h>0 represented the filtering coefficient, which was commonly used to modulate the extent of filtering attenuation. While the NLM algorithm effectively suppressed speckle, it was accompanied by side effects such as edge blurring and information loss.

C. Regional Guidance Multiscale Joint Filtering

The RG-MSJF method differed from traditional NLM techniques in two principal ways, aiming to enhance speckle suppression and preserve edge details within the filtering framework.

- The integration of RGI into the filtering process: This
 approach effectively addressed the issue of edge loss
 by applying partitioned filtering based on RGI, thereby
 minimizing its adverse effects on the filtering results.
- 2) The replacement of the single Euclidean distance metric with a multiscale feature metric: Given the diverse terrain information present in images, it was essential to adopt a multiscale, multiangle, and multirange similarity measurement to more accurately capture the complexity of the data.

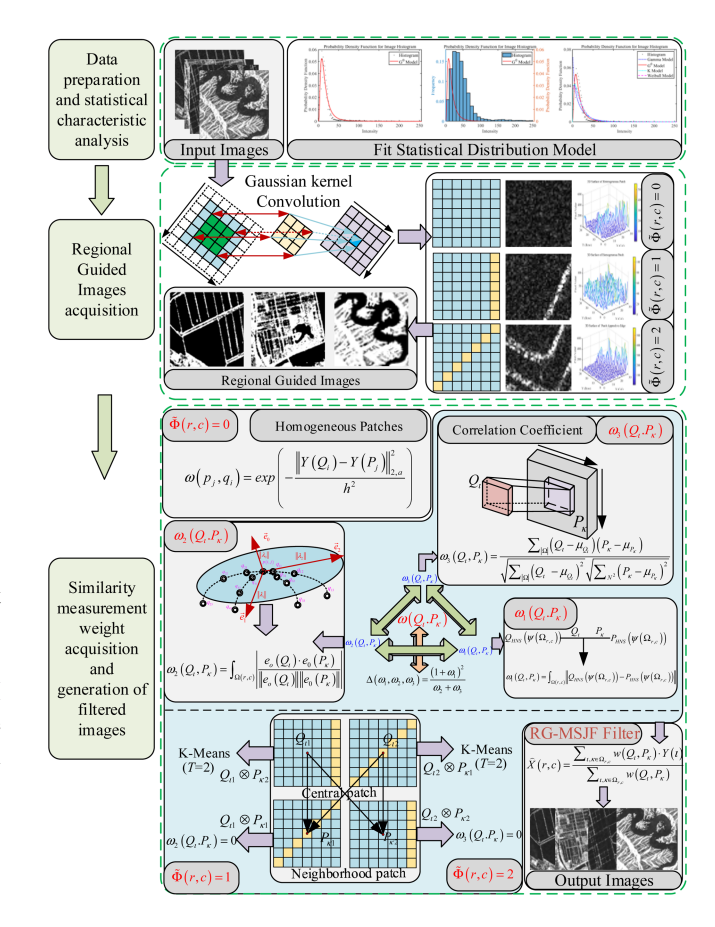


Fig. 3. Flowchart of the RG-MSJF method.

Fig. 3 presents the flowchart of the proposed algorithm. The following are the main steps of RG-MSJF.

Step 1: For a SAR image defined within region $\Omega \subseteq \Re^2$, a NL strategy was employed to construct the RGI. Specifically, for each pixel (r,c) under evaluation, a reference neighborhood $\Omega_{r,c}$ was utilized to generate the final partition outcome. The detailed RGI model is presented as follows:

$$\tilde{\Phi}(r,c) = \operatorname{sign}\left(\exp\left(-\frac{\sum_{\Theta \subseteq \Omega_{r,c}} |\nabla G_{\sigma} \otimes Y_{\Theta}|^2}{T}\right)\right). \quad (7)$$

Here, ∇ denoted the gradient operator; Θ represents the subblock of $\Omega_{r,c}$. G_σ signified the Gaussian kernel function; and \otimes represented the convolution operation. The parameter T>0 functioned as an adjustment variable, designed to stabilize the output across varying regions of the image. It was assigned a higher value in homogeneous patches—where pixel values were relatively uniform—and a lower value in heterogeneous patches, where significant transitions occurred between different pixel values. This adaptive approach ensured that the output remained consistent and controlled according to the local characteristics of the image. The term $\tilde{\Phi}(r,c)$ indicated the category or class to which the pixel (r,c) was assigned. To mitigate artifacts and enhance filtering quality as much as possible, it was proposed to categorize edge regions into a distinct class. The function $\mathrm{sign}(\cdot)$,

which served as a sign indicator, was defined as follows:

$$sign(x) = \begin{cases} 0, & x \ge 1e - 2\\ 1, & 1e - 6 < x < 1e - 2\\ 2, & x \le 1e - 6 \end{cases}$$
 (8)

In this classification scheme, Category 0 denoted homogeneous patches; Category 2 signified heterogeneous patches; and Category 1 referred to edge-adjacent areas, where the central pixel did not lie directly on the boundary. The RGI derived from the aforementioned strategy served as a crucial reference for subsequent filtering experiments.

Step 2: To better capture the intrinsic characteristics of SAR images in the similarity measurement metrics of NL algorithms, similarity evaluation indicators were developed from a multiscale feature perspective. Drawing on the statistical properties of SAR imagery, previous experiments confirmed that, compared to alternative distribution models, the G^0 distribution provided a superior fit for SAR images. Specifically, for a given SAR image, using the G^0 distribution to model heterogeneous patches yielded more effective results than modeling homogeneous regions. The JSD served as a robust metric to quantify the discrepancy between the fitted G^0 distribution and the SAR image histogram. To accurately assess the effectiveness of the G^0 model in fitting heterogeneous patches, the concept of the HNS was introduced. The HNS consisted of three components: the true membership degree, the indeterminate (or uncertain) membership degree, and the false membership degree [44]. These components were used to represent the degree of uncertainty inherent in complex information. The formal definition of the HNS is provided as follows:

$$M = \left\{ \tilde{t}(a), \tilde{i}(a), \tilde{f}(a) | a \in A \right\}. \tag{9}$$

Here, $\tilde{t}(a)$, $\tilde{i}(a)$, and $\tilde{f}(a)$ correspond to the true membership degree, indeterminate (or uncertain) membership degree, and false membership degree, respectively, of an element a belonging to the set M. The HNS $P_{\text{HNS}}(r,c)$ is defined as follows:

$$P_{\text{HNS}}(r,c) = \frac{1}{2} \xi_{\Omega_{r,c}} \left(\lambda_1 | \lambda_2 | 1 - \lambda_1 \right) + \frac{1}{2} \psi_{\Omega_{r,c}} \left(\eta_1 | \eta_2 \right). \tag{10}$$

In this context, the intelligent sets $\xi_{\Omega_{r,c}}$ and $\psi_{\Omega_{r,c}}$ were established within the double hesitation framework. Set $\xi_{\Omega_{r,c}}$ captured the membership degree of speckle points associated with edge points in the SAR image, while set $\psi_{\Omega_{r,c}}$ encapsulated the background information of the image. The term λ_1 denoted the JS distance between the fitted G^0 distribution and the histogram of the SAR image, which was formulated as follows:

$$\lambda_1 = JSD\left(G_I^0(Y) | Hist(Y)\right). \tag{11}$$

The λ_2 metric leveraged the spectral entropy of SAR images to assess the uncertainty of speckle associated with edge points. Spectral entropy, a measure widely used in remote sensing image analysis, is commonly employed to represent the complexity of spectral information present in signals or images [45], [46]. Terrains with greater complexity typically exhibited higher spectral entropy values, whereas smoother and more homogeneous

terrains displayed lower values. The precise formula for this calculation is as follows:

$$\lambda_2(X) = -\int_{-\infty}^{+\infty} f(x) \log(f(x)) dx \tag{12}$$

where f(x) represents the pdf of the signal x, with the pdf of the G^0 distribution utilized. The term $1-\lambda_1$ characterizes the false membership degree of $\xi_{\Omega_{r,c}}$. To derive the final hesitant membership value, the three membership degrees were modeled as follows:

$$\xi_{\Omega_{r,c}} = \frac{\lambda_2 \left(1 - \lambda_1 \right)}{1 + \lambda_1^2}.\tag{13}$$

In the HNS $\psi_{\Omega_{r,c}}$, the elements η_1 and η_2 jointly defined the background characteristics of the image. Here, η_1 represented the contrast information, while η_2 denoted the coefficient of variation of the image. The detailed computations for these parameters were presented as follows:

$$\eta_{1} = \sqrt{\frac{1}{R^{2}} \sum_{a=-R}^{a=R} \sum_{b=-R}^{b=R} (Y(r+a), (c+b) - \mu_{\Omega(r,c)})}$$
(14)

$$\eta_2 = \frac{\sigma\left(\Omega_{r,c}\right)}{\mu\left(\Omega_{r,c}\right)} \tag{15}$$

where $\sigma(\Omega_{r,c})$ and μ $(\Omega_{r,c})$ denote the standard deviation and mean of the search window, respectively, and R represents the radius of the similar window. The membership degree of the HNS $\psi(\Omega_{r,c})$ was expressed as follows:

$$\psi(\Omega_{r,c}) = \eta_1 \log 2 (2 + \eta_2).$$
 (16)

Based on this, the first similarity measure $\omega_1(Q_\iota,P_\kappa)$ of the RG-MSJF model was calculated. The similarity measure ω_1 ranged from 0 to 1, where smaller values indicated higher similarity, and larger values indicated lower similarity

$$\omega_1(Q_\iota, P_\kappa) = \int_{\Omega(r,c)} \|Q_{\text{HNS}}(\psi(\Omega_{r,c})) - P_{\text{HNS}}(\psi(\Omega_{r,c}))\|.$$
(17)

The second similarity measure incorporated a surface variation strategy, which was highly effective in distinguishing flat from uneven areas. Specifically, in homogeneous regions of SAR images, fitting pixel values onto a three-dimensional surface revealed that small variations corresponded to flat areas. In contrast, heterogeneous regions exhibited large differences in pixel values, indicative of uneven areas. Thus, surface variation techniques provided a robust indicator for quantifying regional similarity.

The framework of the surface variation strategy is illustrated in Fig. 4. Neighboring pixel values were selected to fit onto a surface. Here, $FS(Q_\iota)$ and $FS(P_\kappa)$ represent the tangent planes of the fitting surfaces corresponding to the central pixel window and the domain window, respectively. By employing principal component analysis and utilizing the covariance matrix, the normal vector \vec{e}_0 of the tangent plane was calculated. The covariance

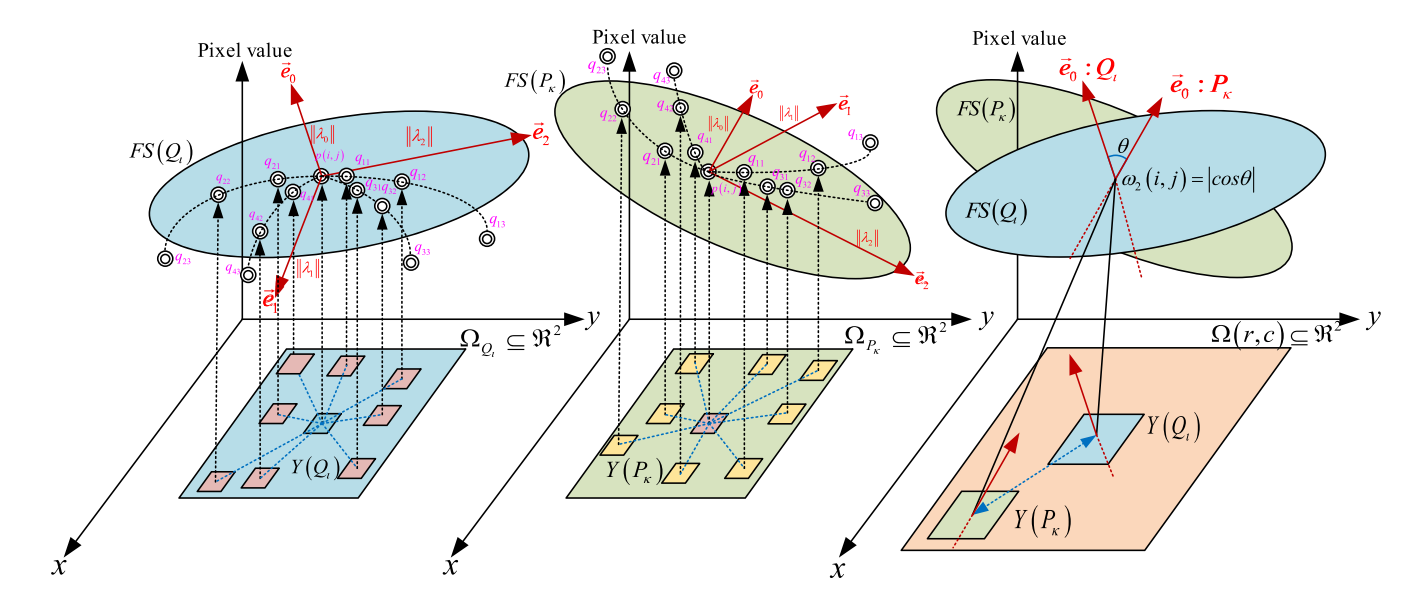


Fig. 4. Framework of the surface variational strategy.

matrix C was constructed as follows:

$$C = \frac{1}{k} \sum_{i=1}^{k} (q_k - \bar{p}) \cdot (q_k - \bar{p})^T$$
 (18)

where k represents the number of selected neighboring pixels, and \bar{p} denotes the mean of the kneighborhoods. The covariance matrix C is a semi-positive definite matrix with eigenvalues $\lambda_0', \lambda_1', \lambda_2' \ (\lambda_0' \leq \lambda_1' \leq \lambda_2')$. The corresponding eigenvectors \vec{e}_0 , \vec{e}_1 , and \vec{e}_2 form an orthogonal coordinate system. The eigenvector \vec{e}_0 can be approximated as the normal vector of the tangent plane. It serves as a measure of the plane's inclination, thereby reflecting the surface's evenness. Based on this, the second similarity metric $\omega_2(Q_\iota, P_\kappa)$ in the RG-MSJF model was calculated

$$\omega_{2}\left(Q_{\iota}, P_{\kappa}\right) = \int_{\Omega(r,c)} \left| \frac{e_{o}\left(Q_{\iota}\right) \cdot e_{0}\left(P_{\kappa}\right)}{\left\|e_{o}\left(Q_{\iota}\right)\right\| \left\|e_{0}\left(P_{\kappa}\right)\right\|} \right|. \tag{19}$$

The similarity measure $\omega_2(Q_\iota,P_\kappa)$ ranges from 0 to 1. Higher values of $\omega_2(Q_\iota,P_\kappa)$ indicate greater similarity between the two patches, while lower values suggest lesser similarity. The third similarity metric employs the correlation coefficient between the central pixel patch and the neighboring patches. The specific model is as follows:

$$\omega_{3}(Q_{\iota}, P_{\kappa}) = \frac{\sum_{|\Omega|} (Q_{\iota} - \mu_{Q_{\iota}}) (P_{\kappa} - \mu_{P_{\kappa}})}{\sqrt{\sum_{|\Omega|} (Q_{\iota} - \mu_{Q_{\iota}})^{2}} \sqrt{\sum_{N^{2}} (P_{\kappa} - \mu_{P_{\kappa}})^{2}}}$$
(20)

where $|\Omega|$ denotes the total number of pixels within the window. The similarity between two patches is quantified using the correlation coefficient, which ranges from 0 to 1. A higher correlation coefficient, approaching 1, signifies a high degree of similarity in the pixel value distributions between the patches. Conversely, a lower correlation coefficient, closer to 0, indicates lesser similarity.

Step 3: Subsequently, the RGI was integrated into the computation of the final weight. The ultimate similarity measurement metric for the RG-MSJF model was formulated as follows:

$$w(Q_{\iota}, P_{\kappa})^{\Phi(r,c)=0} = \exp\left(-\frac{\|Y(Q_{\iota}) - Y(P_{\kappa})\|_{2,a}^{2}}{h^{2}}\right)$$
(21)

$$w(Q_{\iota}, P_{\kappa})^{\Phi(r,c)=1} = \begin{cases} \exp\left(-\frac{\zeta \cdot \Delta(\omega_{1}, \omega_{2}, \omega_{3})}{h^{2}}\right) \Big|_{\Phi(Q_{\iota}) = \Phi(P_{\kappa})}^{T(\Omega_{r,c})} \\ 0\Big|_{\Phi(Q_{\iota}) \neq \Phi(P_{\kappa})} \end{cases}$$
(22)

$$w(Q_{\iota}, P_{\kappa})^{\Phi(r,c)=2} = \begin{cases} \exp\left(-\frac{\zeta \cdot \Delta(\omega_{1}, \omega_{2}, \omega_{3})}{(0.8 \cdot h)^{2}}\right) \Big|_{\Phi(Q_{\iota}) = \Phi(P_{\kappa})}^{T(\Omega_{r,c})} \\ 0\Big|_{\Phi(Q_{\iota}) \neq \Phi(P_{\kappa})} \end{cases}$$
(23)

where ζ is a moderating variable used to control the output within a reasonable range, and $T(\Omega_{r,c})$ represents the number of clusters. $\Phi(Q_\iota) = \Phi(P_\kappa)$ represents that the central sub block and the domain sub-block belong to the same RGI category. $\Phi(Q_\iota) \neq \Phi(P_\kappa)$ represents different categories. A two-cluster strategy was employed to focus on preserving and calculating the similarity of pixels that are similar to the central pixel. For dissimilar pixels, the similarity calculation was omitted. The model for $\Delta(\omega_1,\omega_2,\omega_3)$ was defined as follows:

$$\Delta\left(\omega_1, \omega_2, \omega_3\right) = \frac{\left(1 + \omega_1\right)^2}{\omega_2 + \omega_3}.\tag{24}$$

In accordance with the aforementioned formula, the RG-MSJF model employed the conventional NL method for filtering homogeneous regions. This approach leveraged the traditional NL method's superior capability in suppressing speckle in such regions. For edge and near-edge regions, a partition-based evaluation strategy was utilized. Specifically, a smaller filtering attenuation coefficient was applied to edge regions to enhance the preservation of edge information. In addition, only pixels

belonging to the same category as the central pixel were considered for similarity measurement, while pixels of different types were excluded. Similarity in this context was determined using the *K*-means clustering method.

D. Parameter Estimation of the G⁰ Model

Parameter estimation for the G^0 distribution remains a significant technical challenge that limits its practical application. Freitas et al. proposed using first- and second-order moments for parameter estimation [47], while Frery et al. suggested employing one-half- and one-fourth-order moments [37]. However, both approaches exhibit reduced fitting accuracy due to their inability to achieve full-range parameter estimation. Moreover, maximum likelihood estimation also fails to yield accurate fitting results, primarily because of the complexity of the nonlinear solution process involved.

To address these challenges, a parameter estimation method based on the Mellin transform and logarithmic cumulants is adopted in this paper. As noted in [48], when the true radar cross-section component of the ground object exhibits certain fluctuations, the second-type statistic based on the Mellin transform treats the speckle component as a "Mellin convolution," which significantly simplifies parameter estimation. The first and second types characteristic functions derived from the Mellin transform are defined as follows:

$$\phi_{X}\left(s\right)=\operatorname{MT}\left[P_{X}^{G^{0}}\left(X\right)\right]\left(s\right)=\int_{0}^{\infty}X^{s-1}P_{X}^{G^{0}}\left(X\right)dX\tag{25}$$

$$\Psi_X(s) = \ln(\phi_X)(s). \tag{26}$$

Calculate the derivative of the second type of characteristic function at s=1, which yields the logarithmic cumulative quantity

$$\tilde{c}_k = \left. \frac{d^k \Psi_X(s)}{ds^k} \right|_{s=1}.$$
(27)

By combining the G^0 distribution, the second type of characteristic function was obtained follows:

$$\Psi_{x}(s) = (s-1)\ln\left(\frac{\gamma}{n}\right) + \ln\left(\Gamma\left(n+s-1\right)\right) + \ln\left(\Gamma\left(-\alpha-(s-1)\right)\right) - \ln\left(\Gamma\left(n\right)\right) - \ln\left(\Gamma\left(-\alpha\right)\right). \tag{28}$$

Then, the logarithmic cumulants of each order corresponding to the G^0 distribution were derived by assuming that $x_1,\,x_2$, ..., x_N are N sample observations

$$\begin{cases} \tilde{c}_{1} = \frac{1}{N} \sum_{i=1}^{N} \ln(x_{i}) \\ \tilde{c}_{k} = \frac{1}{N} \sum_{i=1}^{N} \ln^{k}(x_{i} - \widehat{c}_{1}) \end{cases}$$
(29)

Among them, $\Phi(\zeta) = d\log(\Gamma(\zeta))/d\zeta$ represents the Digamma function, and $\Phi(k,\zeta) = d^k\lambda o\gamma(\Gamma(\zeta))/d\zeta^k$ represents the kth order Polygamma function. The estimated expressions for the parameters L,γ , and α of the G^0 distribution

are as follows:

$$\begin{cases}
ln\left(\frac{\gamma}{\widehat{n}}\right) + \Phi\left(\widehat{n}\right) - \Phi\left(-\widehat{\alpha}\right) = \frac{1}{N} \sum_{i=1}^{N} ln\left(x_{i}\right) \\
\Phi\left(1,\widehat{n}\right) + \Phi\left(1,-\widehat{\alpha}\right) = \frac{1}{N} \sum_{i=1}^{N} ln^{2}\left(x_{i}-\widehat{c}_{1}\right). \\
\Phi\left(2,\widehat{n}\right) - \Phi\left(2,-\widehat{\alpha}\right) = \frac{1}{N} \sum_{i=1}^{N} ln^{3}\left(x_{i}-\widehat{c}_{1}\right).
\end{cases} (30)$$

E. Algorithm

Based on the presented derivations, the proposed algorithm called RG-MSJF is summarized in Algorithm 1.

Algorithm 1: RG-MSJF Algorithm.

Input: SAR Image Y, the search window size N, similarity window size M, the filtering attenuation coefficient h

Step:

For all patches to be filtered

For all patches in the search window

- 1). Determine the category $\tilde{\Phi}(P_{\kappa})$ and $\tilde{\Phi}(Q_{\iota})$ to which plaques Q_{ι} and P_{κ} belong
- 2). Calculate HNS through (10). Generate the first metric $\omega_1(Q_\iota, P_\kappa)$ based on (17).
 - 3). Calculate weight $\omega_2(Q_\iota, P_\kappa)$ according to (19).
- 4). Calculate weight $\omega_3(Q_\iota, P_\kappa)$ according to (20).
- 5). Calculate weight $w(Q_{\iota}, P_{\kappa})$ according to (21) to (23).

End for

Compute the estimated value:

$$\widehat{X}(r,c) = \frac{\sum_{\iota,\kappa \in \Omega_{r,c}} w(Q_{\iota}, P_{\kappa}) \cdot Y(\iota)}{\sum_{\iota,\kappa \in \Omega_{r,c}} w(Q_{\iota}, P_{\kappa})}$$
(31)

End for

Return: de-speckled image X(r,c)

III. EXPERIMENT PARAMETERS AND ANALYSIS

This section presents an experimental analysis of the proposed RG-MSJF algorithm. First, the SAR filtering models used for comparison were introduced. Next, the quality assessment methods employed were described. Finally, the parameter settings of the proposed algorithm were thoroughly discussed, followed by detailed analyses.

A. Comparison Algorithms

As discussed in Section I, numerous SAR denoising models have been proposed. To comprehensively evaluate the performance of the proposed algorithm, six filtering models were selected for comparative experiments, namely NLM [29], PPB [31], FANS [34], SRAD [20], SARBM3D [33], SAR-NNFN [7], and EnLee [10].

B. Quantitative Indexes

Quantitative evaluation is essential for verifying the effectiveness of SAR filtering algorithms. In recent years, numerous methods for SAR speckle assessment have been proposed. An

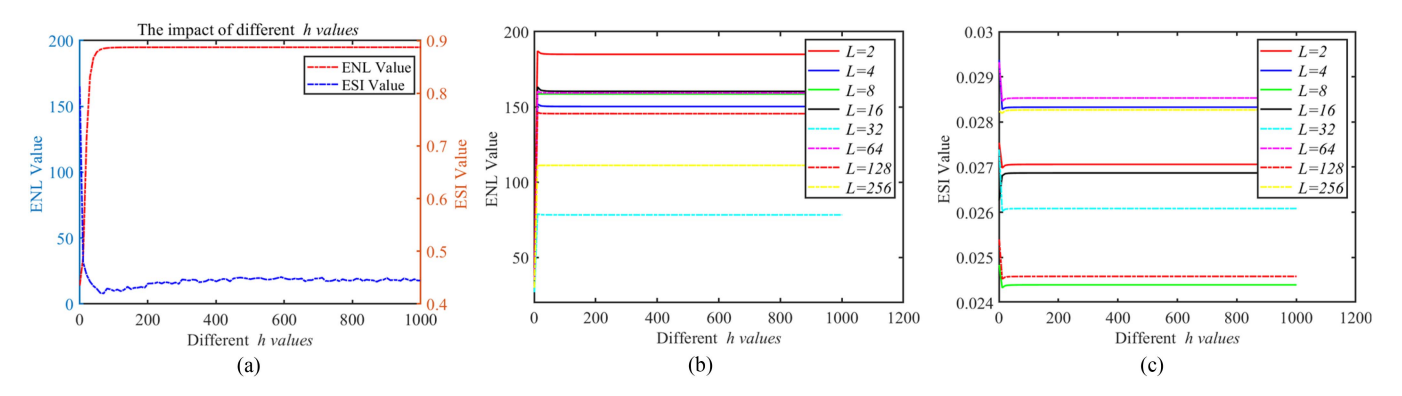


Fig. 5. Influence of parameter h on the filtering results of real and simulated SAR images. (a) ENL and ESI indicators for the real SAR image. (b) and (c) ENL and ESI indicators for the simulated SAR images.

effective speckle suppression model should balance speckle smoothing with edge preservation. Accordingly, the following evaluation indicators were employed in the experiment.

- 1) Equivalent number of looks (ENL) [9]: ENL measures the level of speckle suppression by computing the ratio of the square of the sample mean to the sample variance in homogeneous regions.
- Edge saving index (ESI) [49]: ESI reflects the edgepreserving capability of the filtering model in both horizontal and vertical directions.
- Coherent equivalent number of looks (CENLs) [50]:
 CENL assesses the speckle smoothing performance by analyzing the correlation between the filtered image and the ratio image.
- 4) Homogeneous evaluation factor (HoEF) [51]: HoEF assesses the speckle smoothing capability of de-speckling models in homogeneous patches using the gradient difference and speckle suppression index, as well as the fuzzy index.
- 5) Heterogeneous evaluation factor (HeEF): HeEF evaluates a model's ability to preserve edge information in heterogeneous patches by analyzing both global and local features.
- 6) *IQE_HHSP*: This metric combines HoEF and HeEF to provide a comprehensive evaluation of SAR image despeckling performance.

C. Parameter Settings

The performance of a despeckling algorithm depends on the settings of several parameters, such as the search window size, filtering attenuation coefficient, and number of iterations. In the proposed RG-MSJF method, the following parameters were configured.

- 1) Search window size N.
- 2) Similar window size M.
- 3) Filter attenuation coefficient h.

The search window and similarity window were set to sizes of 15×15 and 7×7 , respectively. Empirical studies have shown that further increasing the window sizes does not significantly improve the final algorithm's performance. These values were

selected to balance computational efficiency and filtering effectiveness, thereby minimizing time complexity while achieving satisfactory results. The parameter h was set to 50. This value is closely related to the degree of speckle smoothing. Since the RG-MSJF method adopts a region-guided filtering strategy and applies lower filtering coefficients specifically to edge patches, a relatively large value of h was chosen. This setting aims to enhance suppression of coherent speckle while minimizing the loss of edge information. To quantitatively evaluate the effect of the h value on filtering performance, ENL and ESI were used as reference indicators. The relationship between h and these indicators is illustrated in Figs. 5 and 6. Specifically, Fig. 5(a) presents results based on real SAR images, while Fig. 5(b) and (c) uses simulated SAR images with different looks. Additional details are provided in Fig. 6.

As depicted in Fig. 5(a), the ENL value consistently increases with risingh, while the ESI index decreases correspondingly before eventually stabilizing. Notably, when h is within the range of $h \in (0, 50]$, both indicators exhibit significant variation. However, for h > 50, the ENL and ESI values remain relatively stable. Based on these findings from real SAR image experiments, it is evident that $h \in [50, 100]$ achieves an optimal balance between speckle suppression and edge preservation in the proposed algorithm. Turning to the simulated SAR image experiments shown in Fig. 6, the ENL index across different looks displays a consistent trend: it increases with growing hwhen $h \in (0, 20]$, and stabilizes thereafter. In contrast, the ESI index shows divergent trends. For images with L=16 and L=256, the ESI index increases, while images with other looks exhibit a decreasing trend. Importantly, the ESI index stabilizes across all look conditions when h > 20. These results suggest that the RG-MSJF model struggles to simultaneously balance speckle suppression and edge preservation when filtering simulated images with L=16 and L=256. Considering the above analysis, the parameter h was set to 50 in the comparative experiments.

IV. EXPERIMENTAL RESULTS AND ANALYSIS

To validate the performance of the proposed algorithm, a series of experiments were conducted on real SAR images, as detailed in the following sections. All experiments were performed

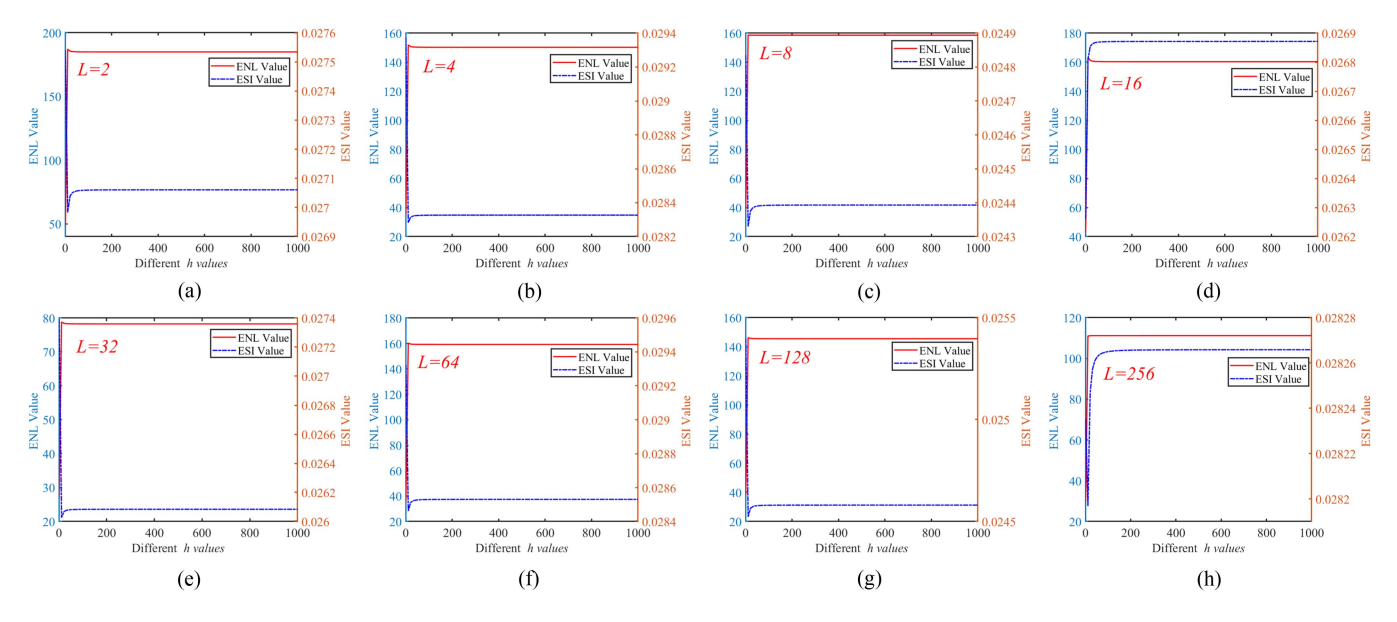


Fig. 6. Influence of parameter h on simulated images with different looks. (a) L=2, (b) L=4, (c) L=8, (d) L=16, (e) L=32, (f) L=64, (g) L=128, (h) L=256.

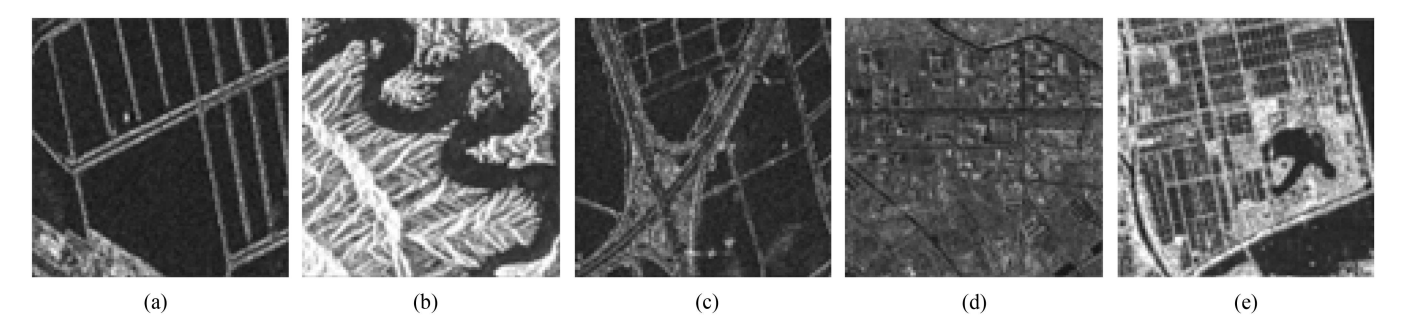


Fig. 7. Real SAR images used in comparative experiments. (a) Ravir. (b) Mountains. (c) Harbor. (d) Roads. (e) Buildings.

GF3\Rivers	ENL	ESI	CENL	HeEF	HoEF	IQE_HHSP
EnLee	14.86	0.19	0.60	0.97	1.49	0.44
NLM	24.64	0.12	0.54	0.96	1.72	0.48
SARBM3D	2.35	0.66	1.57	0.99	0.12	0.18
SRAD	18.29	0.09	0.57	0.77	1.48	0.41
PPB	19.67	0.22	0.51	0.95	1.74	0.48
FANS	26.47	0.30	0.49	0.97	1.88	0.51
SARNNFN	4.62	0.51	1.50	0.06	0.16	0.06
RG-MSJF	34.26	0.27	0.46	0.98	2.34	0.58

TABLE I RIVER EVALUATION INDICATORS

using MATLAB R2022a in an environment configured with an Intel i7 processor, 16 cores, and an NVIDIA RTX 4060 graphics card. The experimental data were obtained from representative regions selected from SAR images captured by GF-3, Sentinel-1, and TerraSAR-X. Both Sentinel-1 and TerraSAR-X datasets are publicly available through their respective official websites. The SAR image used in this study is shown in Fig. 7. For all comparative algorithms, parameter settings followed the default values specified in their respective source literature.

A. Experiment on GF-3 Images

Initially, despeckling experiments were conducted on selected regions of GF-3 images, such as river and harbor areas. The results of these experiments are illustrated in Tables I and II. In these tables, the best-performing values are highlighted in bold.

1) River: Visually, all eight filtering models demonstrate a degree of effectiveness in speckle suppression; however, their performance varies significantly. As shown in the magnified region of Fig. 8, PPB and RG-MSJF exhibit the most

GF3\ Harbour	ENL	ESI	CENL	HeEF	HoEF	IQE_HHSP
EnLee	38.23	0.15	0.63	0.95	1.53	0.53
NLM	55.98	0.09	0.57	0.92	1.74	0.57
SARBM3D	4.14	0.66	1.6	0.99	0.11	0.20
SRAD	46.65	0.08	0.60	0.73	1.51	0.50
PPB	60.73	0.21	0.56	0.98	1.72	0.57
FANS	73.71	0.30	0.54	0.97	1.82	0.59
SARNNFN	4.73	0.53	1.48	0.32	0.18	0.12
RG-MSIF	78.70	0.25	0.53	0.98	2.28	0.69

TABLE II HARBOR EVALUATION INDICATORS

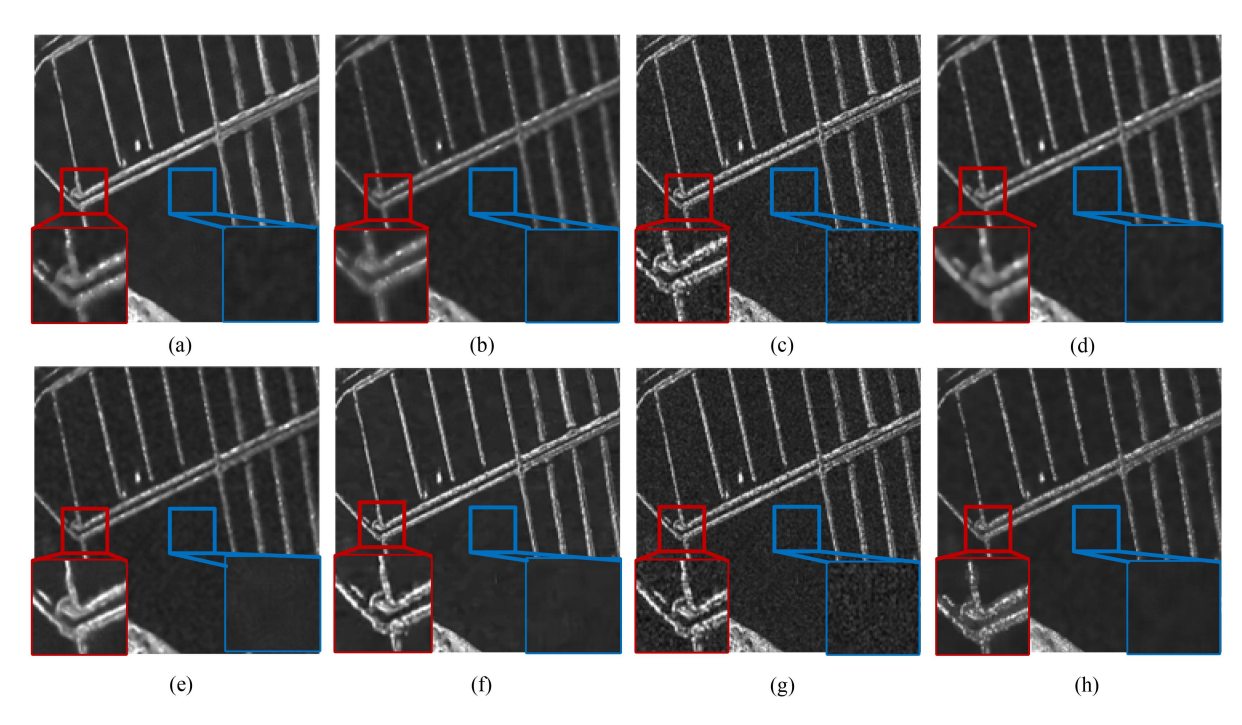


Fig. 8. Comparison of RG-MSJF with popular methods for de-speckling a river image. (a) EnLee. (b) NLM. (c) SARBM3D. (d) SRAD. (e) PPB. (f) FANS. (g) SAR-NNFN. (h) RG-MSJF.

effective smoothing, with a superior ability to eliminate speckle. FANS, EnLee, NLM, and SRAD follow, achieving moderate smoothing, although some surface roughness remains visible. In contrast, SARBM3D and SAR-NNFN demonstrate the least effective suppression, with residual speckle remaining prominent. Regarding edge preservation, EnLee, NLM, FANS and SRAD suffer from noticeable detail blurring and poor retention of edge structures. Conversely, PPB and RG-MSJF effectively preserve edge information while maintaining smoothness. However, PPB introduces noticeable pseudo-texture artifacts. SARBM3D and SAR-NNFN preserve edge features well but do so at the expense of speckle suppression. From a quantitative perspective, RG-MSJF ranks highest in ENL, CENL, and HoEF metrics, indicating its superior performance in both speckle suppression and structural fidelity. SARBM3D and SAR-NNFN perform best in the ESI index, reflecting their focus on edge preservation, yet their relatively low scores in ENL, CENL, and HoEF suggest a tradeoff in overall speckle suppression. In

summary, RG-MSJF and PPB achieve the best and second-best overall rankings, respectively. In contrast, the edge-focused strategies employed by SARBM3D and SAR-NNFN result in lower performance on the comprehensive IQE_HHSP metric.

2) Harbor: Visually, all eight filtering models demonstrated some degree of coherent speckle suppression. As illustrated in the blue-highlighted region of Fig. 9, FANS and RG-MSJF stand out with superior speckle suppression performance, whereas the other six models exhibit undersmoothing. However, both FANS, PPB and NLM introduce noticeable artifacts into the filtered images. In the red-marked extended region, EnLee, NLM, and SRAD show significant edge blurring, indicating a loss of structural detail. The quantitative results presented in Table II are consistent with these visual observations. The proposed RG-MSJF model achieves the best performance in speckle suppression within homogeneous regions and ranks second in edge preservation within heterogeneous regions, thus effectively balancing speckle reduction and texture retention. However,

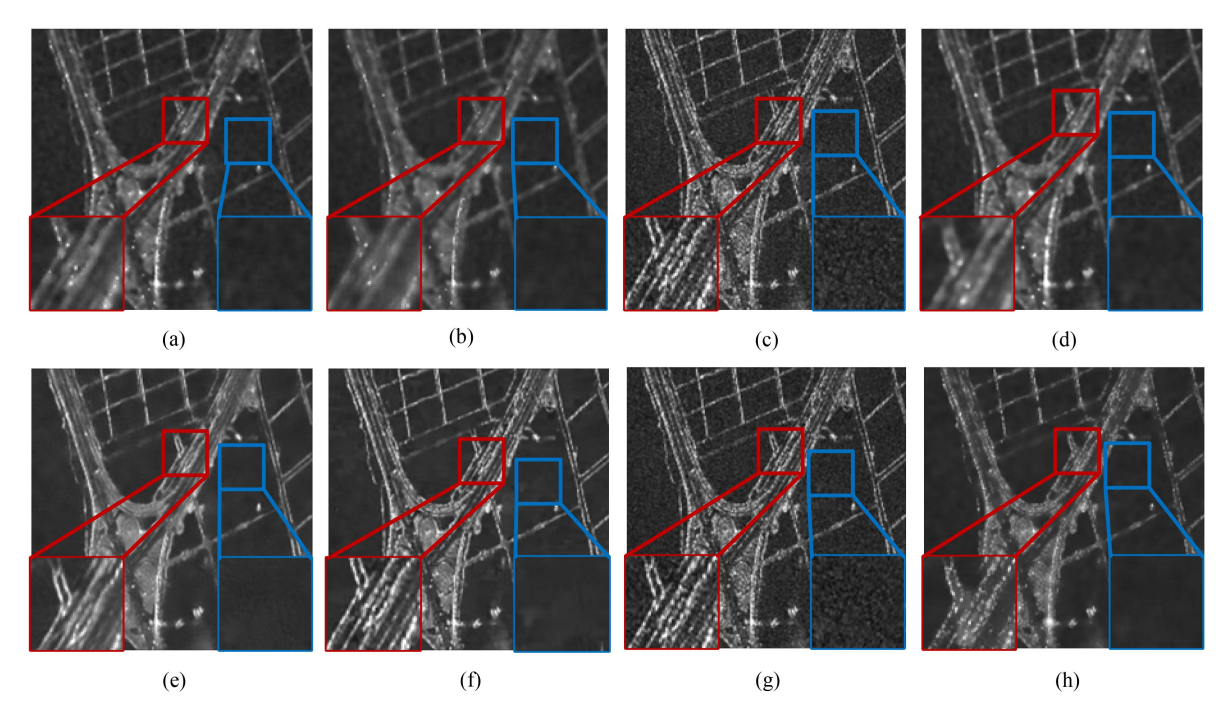


Fig. 9. Comparison of RG-MSJF with popular methods for de-speckling a harbor image. (a) EnLee. (b) NLM. (c) SARBM3D. (d) SRAD. (e) PPB. (f) FANS. (g) SAR-NNFN. (h) RG-MSJF.

Sen-1\Roads	ENL	ESI	CENL	HeEF	HoEF	IQE_HHSP
EnLee	92.60	0.19	0.51	0.35	0.96	5.22
NLM	137.33	0.11	0.47	0.15	1.03	4.88
SARBM3D	23.01	0.48	0.73	0.41	0.20	4.85
SRAD	114.09	0.11	0.49	0.11	0.94	4.74
PPB	335.45	0.11	0.40	0.24	1.32	5.24
FANS	71.12	0.22	0.54	0.33	0.64	4.98
SARNNFN	517.46	0.14	0.37	0.15	1.46	5.16
RG-MSJF	204.74	0.16	0.43	0.37	1.34	5.44

TABLE III ROADS EVALUATION INDICATORS

its ESI value is slightly lower than those of SARBM3D and SAR-NNFN, both of which prioritize edge preservation at the cost of speckle suppression. FANS and PPB strike a balance between speckle suppression and edge preservation; however, their tendency to generate false textures undermines any advantage they might otherwise offer in these two metrics. The HeEF score of RG-MSJF is comparable to that of PPB, whereas SAR-NNFN exhibits the poorest performance in this metric. In terms of comprehensive evaluation, the IQE_HHSP metric indicates that RG-MSJF achieves the highest overall ranking, demonstrating robust and balanced performance across all assessed criteria. FANS ranks just behind RG-MSJF in overall performance. NLM and PPB yield comparable results, achieving a reasonable balance between speckle suppression and edge preservation. EnLee and SRAD perform slightly worse than NLM and PPB, while SAR-NNFN ranks lowest, suggesting that its emphasis on edge preservation compromises overall image quality. Overall, the proposed RG-MSJF model demonstrates a favorable tradeoff between speckle reduction and edge retention.

B. Experiment on Sentinel-1 Images

Next, filtering experiments were conducted on road and mountainous regions within Sentinel-1 images. The filtering results are illustrated in Figs. 10 and 11, with the corresponding quantitative evaluation results provided in Tables III and IV. In these tables, the best-performing values are highlighted in bold.

1) Roads: Visually, all eight filtering models achieved a certain degree of coherent speckle suppression. EnLee, NLM, FANS, and SARBM3D exhibit noticeable undersmoothing, with residual speckle remaining in the filtered images. In contrast, PPB and SAR-NNFN effectively suppress coherent speckle, producing smoother textures. RG-MSJF stands out by successfully preserving detailed information, maintaining both texture and structural integrity. From a quantitative perspective, the evaluation results are consistent with the visual observations. SAR-NNFN attains the highest scores in the ENL and CENL metrics, reflecting strong speckle suppression capability. However, its ESI and HeEF scores are relatively poor, indicating

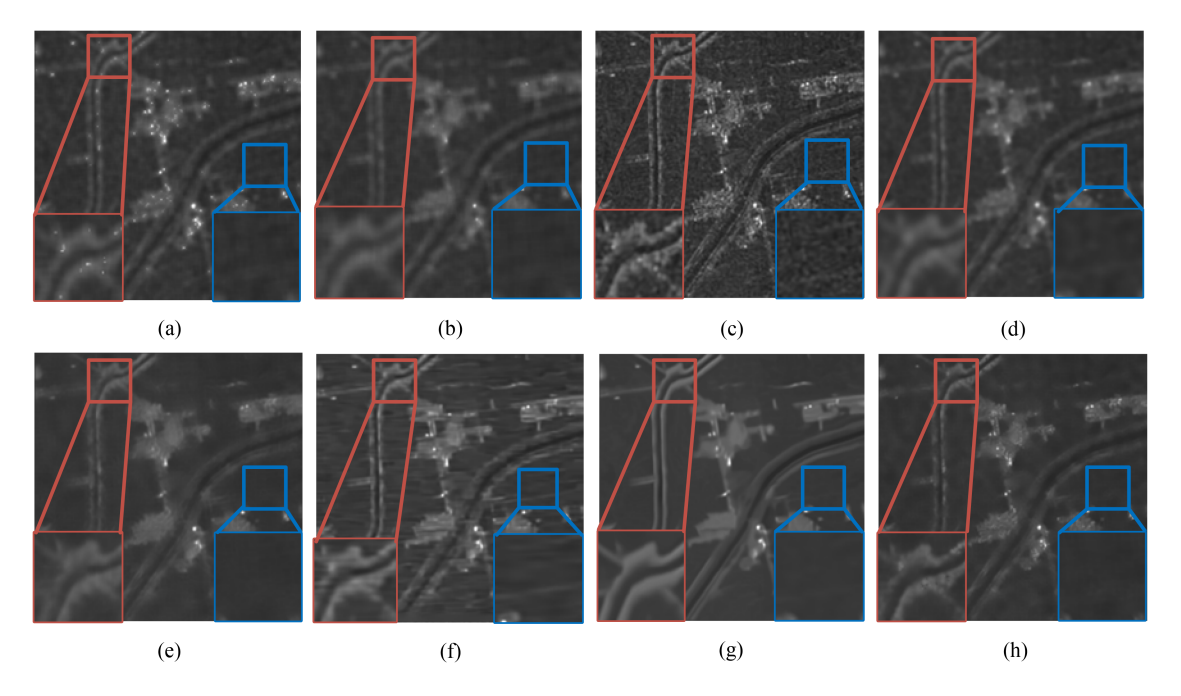


Fig. 10. Comparison of RG-MSJF with popular methods for de-speckling a road image. (a) EnLee. (b) NLM. (c) SARBM3D. (d) SRAD. (e) PPB. (f) FANS. (g) SAR-NNFN. (h) RG-MSJF.

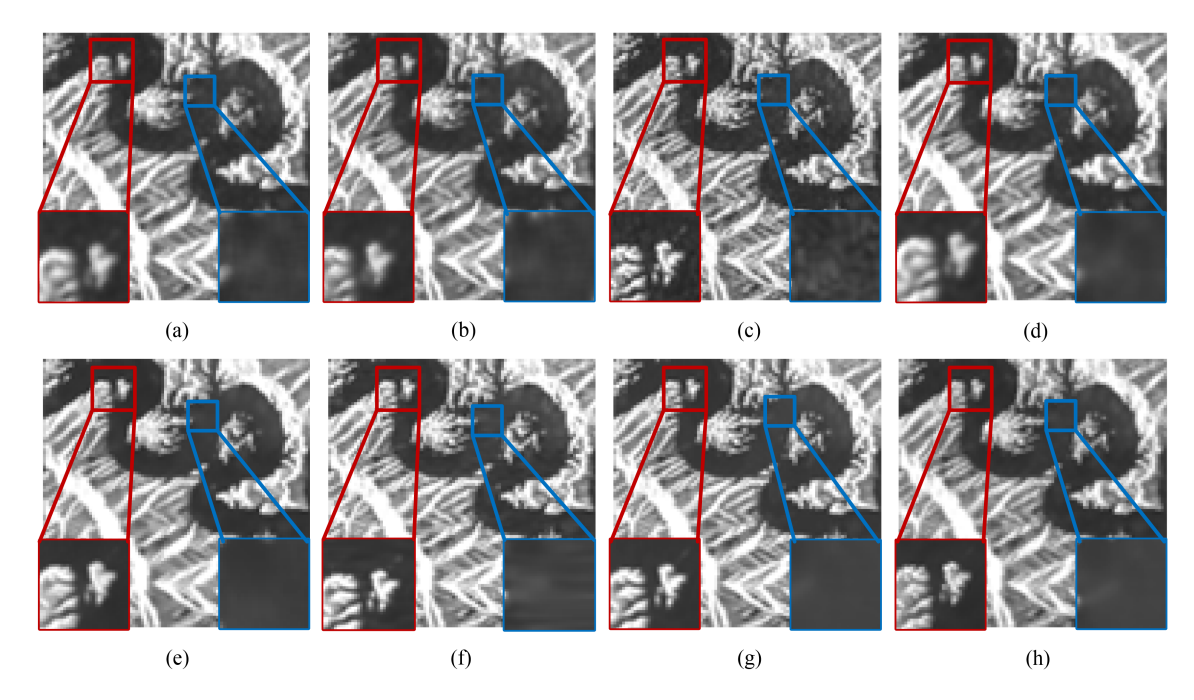


Fig. 11. Comparison of RG-MSJF with popular methods for de-speckling a mountain image. (a) EnLee. (b) NLM. (c) SARBM3D. (d) SRAD. (e) PPB. (f) FANS. (g) SAR-NNFN. (h) RG-MSJF.

excessive smoothing and a loss of fine details. FANS and EnLee excel at edge preservation, yet their comparatively modest noise suppression curtails their IQE_HHSP scores. RG-MSJF excels in the HoEF metric and the comprehensive evaluation index (IQE_HHSP), due to its balanced performance in both speckle suppression and information preservation. While PPB is effective in reducing speckle, it introduces some false texture artifacts, resulting in slightly lower overall performance compared to RG-MSJF.

2) Mountains: Visually, all eight filtering models suppressed coherent speckle in mountain images. EnLee, NLM, and SRAD exhibited smooth transitions in the filtered images. FANS, PPB, SARNNFN, and RG-MSJF achieved a good balance between speckle suppression and edge preservation. In contrast, SARBM3D demonstrated relatively poor speckle suppression. Regarding evaluation metrics, SARNNFN attained the best results in ENL and CENL, indicating strong speckle suppression capabilities; however, its performance on edge-related metrics,

Sen-1\ Mountains	ENL	ESI	CENL	HeEF	HoEF	IQE_HHSP
EnLee	11.66	0.32	0.94	0.81	0.60	3.53
NLM	13.60	0.30	0.88	0.81	0.75	3.69
SARBM3D	4.77	0.68	1.47	0.85	0.15	2.96
SRAD	11.95	0.21	0.93	0.36	0.61	3.32
PPB	16.12	0.31	0.83	0.60	0.89	3.72
FANS	8.26	0.48	1.09	0.80	0.42	3.31
SARNNFN	17.73	0.22	0.80	0.07	0.84	3.38
RG-MSJF	10.77	0.48	0.97	0.57	0.85	3.67

TABLE IV
MOUNTAINS EVALUATION INDICATORS

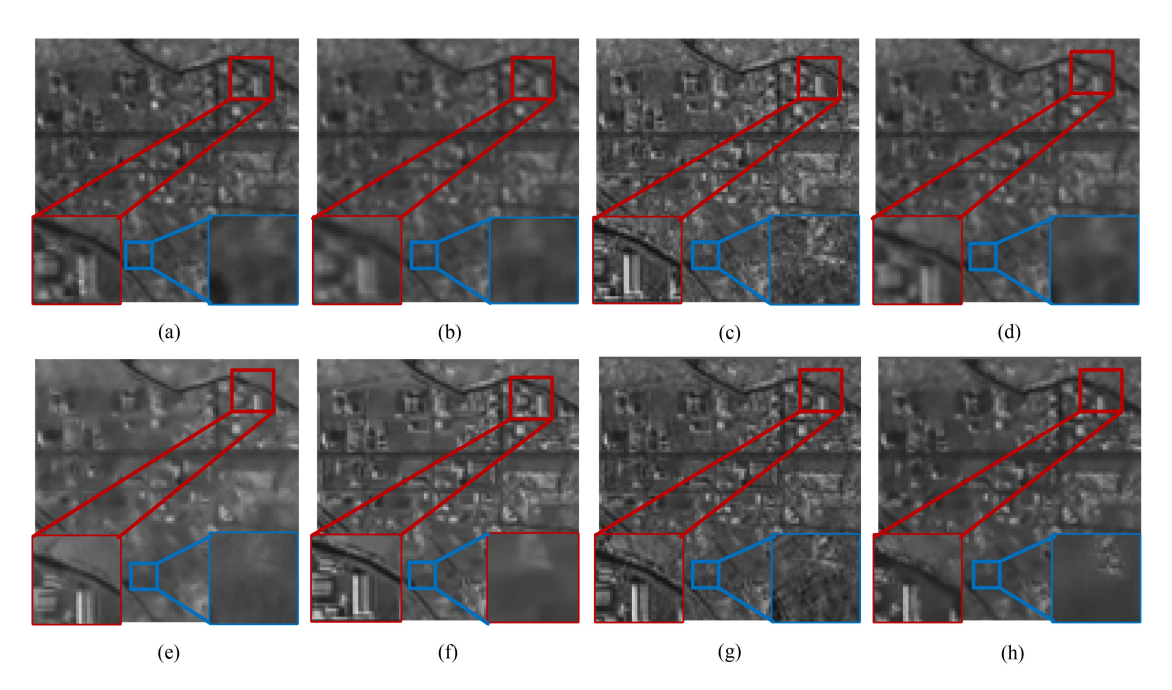


Fig. 12. Comparison of RG-MSJF with popular methods for de-speckling a building image. (a) EnLee. (b) NLM. (c) SARBM3D. (d) SRAD. (e) PPB. (f) FANS. (g) SAR-NNFN. (h) RG-MSJF.

such as HeEF and ESI, was less favorable. FANS exhibits pronounced pseudo-texture artifacts, which reduces their edge preservation ability. SARBM3D showed the opposite trend, performing well in edge metrics but poorly in speckle suppression metrics. Both PPB and RG-MSJF consistently ranked among the top across all indicators, demonstrating their effectiveness in balancing speckle suppression and edge preservation. The traditional NLM model showed no significant advantage in either speckle suppression or edge preservation. Considering comprehensive indicators, PPB and RG-MSJF exhibited the best overall performance, followed by NLM, SARNNFN, EnLee, SRAD, and FANS. SARBM3D ranked lowest. The RG-MSJF model proposed in this article was validated both visually and through quantitative metrics, confirming its effectiveness and advancement in filtering mountain images.

C. Experiment on Terra-SAR X Image

Finally, filtering experiments were conducted on specific areas, including buildings and roads, in the TerraSAR-X image.

The results are visually presented in Fig. 12. Corresponding quantitative evaluation indicators are detailed in Table V, with optimal values highlighted in bold for clarity.

1) Buildings and Roads: As illustrated in Fig. 12, the filtering results revealed distinct characteristics among the models. EnLee, SRAD, and NLM continued to exhibit pronounced over-smoothing, resulting in a loss of fine details. PPB and FANS displayed noticeable false textures, which were visually distracting. Meanwhile, SARBM3D and SARNNFN retained more residual speckle compared to the other models.

From the perspective of quantitative evaluation, EnLee, SRAD, and NLM demonstrated a significant advantage in the ENL indicator, reflecting strong speckle suppression capabilities. However, this advantage came at the cost of oversmoothing, as evidenced by their poorer performance in the HoEF indicator. This tradeoff aligned with visual observations, where excessive smoothing caused the loss of important structural information.

SARBM3D and SARNNN, conversely, achieved better results in the ESI and HeEF indicators, highlighting their ability

TSX-2\Buildings	ENL	ESI	CENL	HeEF	HoEF	IQE_HHSP
EnLee	16.88	0.10	0.81	0.27	0.60	7.99
NLM	30.19	0.06	0.68	0.13	0.75	7.98
SARBM3D	2.95	0.69	2.13	0.43	0.15	6.80
SRAD	25.15	0.04	0.71	0.15	0.61	7.85
PPB	26.13	0.15	0.71	0.27	0.89	8.05
FANS	17.68	0.26	0.78	0.37	0.85	7.94
SARNNFN	3.99	0.46	1.66	0.42	0.84	7.36
RG-MSJF	10.49	0.31	0.98	0.39	0.85	8.02

TABLE V
BUILDINGS EVALUATION INDICATORS

to preserve edges and details. Nevertheless, their strategy of prioritizing edge preservation over speckle suppression was not advisable, as indicated by its lowest ranking in the comprehensive indicator IQE_HHSP. Sacrificing speckle suppression for edge preservation resulted in suboptimal overall performance.

The proposed RG-MSJF model, while not the top performer in any single indicator, demonstrated balanced performance. It effectively suppressed speckle while preserving most edge information, as evidenced by its second-place overall ranking. This balanced approach ensured that the model maintained an adequate level of detail without excessive smoothing or speckle retention, making it a robust choice for filtering applications. These results substantiate the model's pronounced efficacy and clear superiority in despeckling of TSX images.

V. CONCLUSION

This article introduces a novel multiscale joint filtering model, termed RG-MSJF, based on region-guided maps. The proposed algorithm integrates traditional NLM filtering models and employs region-guided images to facilitate partitioned filtering. This approach effectively mitigates the adverse effects of speckle suppression on edge information, a common issue in conventional filtering models. By fully leveraging multiscale features—including spatial pixel information and statistical image characteristics—it reconstructs the similarity measurement index of NLM. The algorithm's efficacy in speckle suppression and detail preservation was rigorously evaluated using various types of ground objects in real SAR images. Experimental results demonstrated that the proposed method is highly competitive compared to mainstream algorithms, effectively suppressing both over-smoothing and under-smoothing while retaining important information. However, a significant limitation of the algorithm is its high computational cost, largely due to the multiple iterations required for G^0 distribution fitting, which increases complexity. For a SAR image of size $W \times H$, the proposed algorithm exhibits a computational complexity of $O(WH(2N+1)^2M^2)$ in its standard implementation. Future research will focus on extending this algorithm to other domains, such as transform-domain filtering and AD filtering, to further enhance its capabilities. Furthermore, integral images and multithreaded parallelism should be integrated to reduce the overall time complexity.

ACKNOWLEDGMENT

The authors express their gratitude to the anonymous reviewers for their valuable comments and insightful suggestions, which significantly contributed to the improvement of this study.

REFERENCES

- L. Xu, P. Liu, and Y.-Q. Jin, "A new nonlocal iterative trilateral filter for SAR images despeckling," *IEEE Trans. Geosci. Remote Sens.*, vol. 62, 2024, Art. no. 5213319.
- [2] F. Guo et al., "Fusion despeckling based on surface variation anisotropic diffusion filter and ratio image filter," *IEEE Trans. Geosci. Remote Sens.*, vol. 58, no. 4, pp. 2398–2411, Apr. 2020.
- [3] P. Singh and R. Shree, "Analysis and effects of speckle noise in SAR images," in *Proc. 2nd Int. Conf. Adv. Comput., Commun.*, & Autom., Nov. 2016, pp. 1–5.
- [4] P. Singh et al., "A review on SAR image and its despeckling," Arch. Comput. Methods Eng., vol. 28, pp. 4633–4653, Feb. 2021.
- [5] S. Xiao, S. Zhang, L. Huang, and W.-Q. Wang, "Trans-NLM Network for SAR image despeckling," *IEEE Trans. Geosci. Remote Sens.*, vol. 62, 2024, Art. no. 5211912.
- [6] W. Ni and X. Gao, "Despeckling of SAR image using generalized guided filter with Bayesian nonlocal means," *IEEE Trans. Geosci. Remote Sens.*, vol. 54, no. 1, pp. 567–579, Jan. 2016.
- [7] F. Bo, X. Ma, Y. Cen, and S. Hu, "SAR image speckle reduction based on nuclear norm minus Frobenius norm regularization," *IEEE Trans. Geosci. Remote Sens.*, vol. 62, 2024, Art. no. 5227915.
- [8] X. Ma, C. Wang, Z. Yin, and P. Wu, "SAR image despeckling by noisy reference-based deep learning method," *IEEE Trans. Geosci. Remote Sens.*, vol. 58, no. 12, pp. 8807–8818, Dec. 2020.
- [9] C. Oliver and S. Quegan, Understanding Synthetic Aperture Radar Images. Boston, MA, USA: Artech House, 1998.
- [10] J.-S. Lee, "Digital image enhancement and noise filtering by use of local statistics," *IEEE Trans. Geosci. Remote Sens.*, vol. PAMI-2, no. 2, pp. 165–168, Mar. 1980.
- [11] J.-S. Lee, "Refined filtering of image noise using local statistics," *Comput. Graph. Image Process.*, vol. 15, no. 4, pp. 380–389, 1981.
- [12] D. T. Kuan, A. A. Sawchuk, T. C. Strand, and P. Chavel, "Adaptive noise smoothing filter for images with signal-dependent noise," *IEEE Trans. Pattern Anal. Mach. Intell.*, vol. PAMI-7, no. 2, pp. 165–177, Mar 1985
- [13] Z. Sun, Z. Zhang, Y. Chen, S. Liu, and Y. Song, "Frost filtering algorithm of SAR images with adaptive windowing and adaptive tuning factor," *IEEE Geosci. Remote Sens. Lett.*, vol. 17, no. 6, pp. 1097–1101, Jun. 2020.
- [14] A. Baraldi and F. Parmiggiani, "A refined gamma MAP SAR speckle filter with improved geometrical adaptivity," *IEEE Trans. Geosci. Remote Sens.*, vol. 33, no. 5, pp. 1245–1257, Sep. 1995.
- [15] P. A. A. Penna and N. D. A. Mascarenhas, "SAR speckle nonlocal filtering with statistical modeling of HAAR wavelet coefficients and stochastic distances," *IEEE Trans. Geosci. Remote Sens.*, vol. 57, no. 9, pp. 7194–7208, Sep. 2019.
- [16] X. Qian et al., "Ridgelet-nets with speckle reduction regularization for SAR image scene classification," *IEEE Trans. Geosci. Remote Sens.*, vol. 59, no. 11, pp. 9290–9306, Nov. 2021.

- [17] D. Devapal, N. Hashna, V. Aparna, C. Bhavyasree, J. Mathai, and K. S. Soman, "Object detection from SAR images based on curvelet despeckling," *Mater. Today, Proc.*, vol. 11, pp. 1102–1116, 2019.
- [18] G. Liu, H. Kang, Q. Wang, Y. Tian, and B. Wan, "Contourlet-CNN for SAR image despeckling," *Remote Sens*, vol. 13, 2021, Art. no. 764.
- [19] S. Liu, M. Liu, P. Li, J. Zhao, Z. Zhu, and X. Wang, "SAR image denoising via sparse representation in shearlet domain based on continuous cycle spinning," *IEEE Trans. Geosci. Remote Sens.*, vol. 55, no. 5, pp. 2985–2992, May 2017.
- [20] Y. Yu and S. T. Acton, "Speckle reducing anisotropic diffusion," *IEEE Trans. Image Process.*, vol. 11, no. 11, pp. 1260–1270, Nov. 2002.
- [21] S. Aja-Fernandez and C. Alberola-Lopez, "On the estimation of the coefficient of variation for anisotropic diffusion speckle filtering," *IEEE Trans. Image Process.*, vol. 15, no. 9, pp. 2694–2701, Sep. 2006.
- [22] F. Guo, C. Zhou, W. Liu, and Z. Liu, "Pixel difference function and local entropy-based speckle reducing anisotropic diffusion," *IEEE Trans. Geosci. Remote Sens.*, vol. 60, 2022, Art. no. 5229516.
- [23] G. Chierchia, D. Cozzolino, G. Poggi, and L. Verdoliva, "SAR image despeckling through convolutional neural networks," in *Proc. IEEE Int. Geosci. Remote Sens. Symp.*, 2017, pp. 5438–5441.
- [24] Q. Zhang, Q. Yuan, J. Li, Z. Yang, and X. Ma, "Learning a dilated residual network for SAR image despeckling," *Remote Sens.*, vol. 10, no. 2, pp. 1–18, Jan. 2018.
- [25] S. Vitale, G. Ferraioli, and V. Pascazio, "Multi-objective CNN-based algorithm for SAR despeckling," *IEEE Trans. Geosci. Remote Sens.*, vol. 59, no. 11, pp. 9336–9349, Nov. 2021.
- [26] S. Vitale, G. Ferraioli, A. C. Frery, V. Pascazio, D. -X. Yue, and F. Xu, "SAR despeckling using multi-objective neural network trained with generic statistical samples," *IEEE Trans. Geosci. Remote Sens.*, vol. 61, 2023, Art. no. 5216812.
- [27] S. Liu, L. Zhang, S. Tian, Q. Hu, B. Li, and Y. Zhang, "MFAENet: A multiscale feature adaptive enhancement network for SAR image despeckling," *IEEE J. Sel. Topics Appl. Earth Observ. Remote Sens.*, vol. 16, pp. 10420–10433, 2023.
- [28] X. Wang, Y. Wu, C. Shi, Y. Yuan, and X. Zhang, "ANED-Net: Adaptive noise estimation and despeckling network for SAR image," *IEEE J. Sel. Topics Appl. Earth Observ. Remote Sens.*, vol. 17, pp. 4036–4051, 2024.
- [29] A. Buades, B. Coll, and J. M. Morel, "A review of image denoising algorithms, with a new one," *Multiscale Model. Simul.*, vol. 4, no. 2, pp. 490–530, Jan. 2005.
- [30] H. Feng, B. Hou, and M. Gong, "SAR image despeckling based on local homogeneous-region segmentation by using pixel-relativity measurement," *IEEE Trans. Geosci. Remote Sens.*, vol. 49, no. 7, pp. 2724–2737, Jul. 2011.
- [31] C.-A. Deledalle, L. Denis, and F. Tupin, "Iterative weighted maximum likelihood denoising with probabilistic patch-based weights," *IEEE Trans. Geosci. Remote Sens.*, vol. 18, no. 12, pp. 2661–2672, Dec. 2009.
- [32] H. Zhong, Y. Li, and L. Jiao, "Bayesian nonlocal means filter for SAR image despeckling," in *Proc. 2nd Asian-Pacific Conf. Synthetic Aperture Radar*, Jan. 2020, pp. 1096–1099.
- [33] S. Parrilli, M. Poderico, C. V. Angelino, and L. Verdoliva, "A nonlocal SAR image denoising algorithm based on LLMMSE wavelet shrinkage," *IEEE Trans. Geosci. Remote Sens.*, vol. 50, no. 2, pp. 606–616, Feb. 2012.
- [34] D. Cozzolino, S. Parrilli, G. Scarpa, G. Poggi, and L. Verdoliva, "Fast adaptive nonlocal SAR despeckling," *IEEE Geosci. Remote Sens. Lett.*, vol. 11, no. 2, pp. 524–528, Feb. 2014.
- [35] G. Ferraioli, V. Pascazio, and G. Schirinzi, "Ratio-based nonlocal anisotropic despeckling approach for SAR images," *IEEE Trans. Geosci. Remote Sens.*, vol. 57, no. 10, pp. 7785–7798, Oct. 2019.
- [36] S. Vitale, D. Cozzolino, G. Scarpa, L. Verdoliva, and G. Poggi, "Guided patchwise nonlocal SAR despeckling," *IEEE Trans. Geosci. Remote Sens.*, vol. 57, no. 9, pp. 6484–6498, Sep. 2019.
- [37] A. C. Frery, H. -J. Muller, C. C. F. Yanasse, and S. J. S. Sant'Anna, "A model for extremely heterogeneous clutter," *IEEE Trans. Geosci. Remote Sens.*, vol. 35, no. 3, pp. 648–659, May 1997.
- [38] J. Feng, Z. Cao, and Y. Pi, "Multiphase SAR image segmentation with G0-statistical-model-based active contours," *IEEE Trans. Geosci. Remote Sens.*, vol. 51, no. 7, pp. 4190–4199, Jul. 2013.
- [39] X. Wang and C. Li, "Multiphase segmentation of SAR images with level set evolution," in *Proc. WRI Glob. Congr. Intell. Syst.*, 2009, vol. 2, pp. 447–452.
- [40] M. Lu, Z. He, and Y. Su, "An active contour model for SAR image segmentation," in *Proc. IET Int. Radar Conf.*, 2009, pp. 1–5.

- [41] M. E. Mejail, A. C. Frery, J. Jacobo-Berlles, and O. H. Bustos, "Approximation of dis tributions for SAR images: Proposal, evaluation and practical consequences," *Latin Amer. Appl. Res.*, vol. 31, pp. 83–92, 2001.
- [42] I. B. Ayed, N. Hennane, and A. Mitiche, "Unsupervised variational image segmentation/classification using a Weibull observation model," *IEEE Trans. Image Process.*, vol. 15, no. 11, pp. 3431–3439, Nov. 2006.
- [43] J. Lin, "Divergence measures based on the Shannon entropy," *IEEE Trans. Inf. Theory*, vol. 37, no. 1, pp. 145–151, Jan. 1991.
- [44] B. Tanuwijaya et al., "A novel single valued neutrosophic hesitant fuzzy time series model: Applications in Indonesian and Argentinian stock index forecasting," *IEEE Access*, vol. 8, pp. 60126–60141, 2020.
- [45] P. A. Tyraskis and O. G. Jensen, "Multichannel linear prediction and maximum-entropy spectral analysis using least squares modeling," *IEEE Trans. Geosci. Remote Sens.*, vol. GE-23, no. 2, pp. 101–109, Mar. 1985.
- [46] A. Rovelli, "On the information time scale of geophysical records in maximum entropy spectral analysis," *IEEE Trans. Geosci. Remote Sens.*, vol. GE-20, no. 2, pp. 158–161, Apr. 1982.
- [47] C. C. Freitas, A. C. Frery, and A. H. Correia, "The polarimetric G distribution for SAR data analysis," *Environmetrics*, vol. 16, no. 1, pp. 13–31, Feb. 2005.
- [48] J. M. Nicolas and F. Tupin, "Gamma mixture modeled with 'second kind statistics': Application to SAR image processing," in *Proc. IEEE Int. Geosci. Remote Sens. Symp.*, 2002, pp. 2489–2491.
- [49] P. J. L.Tang and C. Dai, "A comparative study of the effectiveness of speckle noise removal methods for satellite-borne SAR images," *Remote Sens. Environ.*, vol. 11, no. 3, pp. 206–211, Aug. 1996.
- [50] F. Guo, C. Sun, N. Sun, X. Ma, and W. Liu, "Integrated quantitative evaluation method of SAR filters," *Remote Sens*, vol. vol. 15, no.no. 5, Mar. 2023, Art. no. 1409.
- [51] C. Sun, F. Guo, Z. Hu, L. Zhang, W. Liu, and T. Huang, "Despeckling SAR image quality evaluation by homogeneity and heterogeneity scene patches," *IEEE J. Sel. Topics Appl. Earth Observ. Remote Sens.*, vol. 17, pp. 19211–19229, 2024.



Chuang Sun was born in 2000. He received the B.E. degree in remote sensing science and technology, in 2026 and the M.S. degree in cartography and geographical information system from Jiangsu Normal University, Xuzhou, China.

He majors in synthetic aperture radar image processing.



Fengcheng Guo was born in 1992. He received the Ph.D. degree in photogrammetry and remote sensing from the State Key Laboratory of Information Engineering in Surveying Mapping, and Remote Sensing (LIESMRS), Wuhan University, Wuhan, China, in 2020

Since 2020, he has been with the School of Geography, Geomatics and Planning, Jiangsu Normal University, where he became an Associate Professor in 2022. He majors in SAR image processing.



Zhaoling Hu was born in 1973. She received the Graduate and Ph.D. degrees in cartography and geographic information systems from China University of Mining and Technology, Xuzhou, China, in 1998.

She has been working with Jiangsu Normal University, Xuzhou, China, since 2001. She was appointed as a Professor, in 2010. Her research interests include remote sensing information extraction and application.



Lianpeng Zhang received the M.S. degree in geodesy and survey engineering from the Shandong University of Science and Technology, Taian, China, in 1989, and the Ph.D. degree in photogrammetry and remote sensing from the Shandong University of Science and Technology, Qingdao, China, in 2003.

He is currently a Professor with the School of Geography, Geomatics and Planning, Jiangsu Normal University, Xuzhou, China. His research interests include high-resolution image processing and computer vision in urban remote sensing applications.



Tingting Huang was born in 2000. She received the B.E. degree of engineering in remote sensing science and technology from Jiangsu Normal University, Xuzhou, China, in 2023. She is currently working toward the M.E. degree in measurement science and technology with Guilin University of Technology, Guilin, China.

She majors in Ocean color remote sensing.



Wensong Liu received the M.S. degree in surveying and mapping from China University of Petroleum, Qingdao, China, in 2016, and the Ph.D. degree in photogrammetry and remote sensing from Wuhan University, Wuhan, China, in 2019.

He is currently an Associate Professor and Researcher with the School of Geography, Geomatics and Planning, Jiangsu Normal University, Xuzhou, China. His research interests include PolSAR images processing and change detection.